To cite this version :

Jean-Christophe HOARAU, Paola CINNELLA, Xavier GLOERFELT - Large eddy simulation of turbomachinery flows using a high-order implicit residual smoothing scheme - Computers & Fluids - Vol. 198, p.104395 - 2020

Computers and Fluids

Large eddy simulation of turbomachinery flows using a high-order implicit residual smoothing scheme

J.-Ch. Hoarau, P. Cinnella*, X. Gloerfelt

DynFluid Laboratory - Arts et Métiers ParisTech - 151 boulevard de l'Hôpital, Paris 75013, France

A B S T R A C T

A recently developed fourth-order accurate implicit residual smoothing scheme (IRS4) is investigated for the large eddy simulation of turbomachinery flows, characterized by moderate to high Reynolds numbers and subject to severe constraints on the maximum allowable time step if an explicit scheme is used. For structured multi-block meshes, the proposed approach leads to the inversion of a scalar pentadiagonal system by mesh direction, which can be done very efficiently. On the other hand, applying IRS4 at each stage of an explicit Runge–Kutta time scheme allows to increase the time step by a factor 5 to 10, leading to substantial savings in terms of overall computational time. With respect to standard second-order fully implicit approaches, the IRS4 does not require approximate linearization and factorization procedures nor inner Newton-Raphson subiterations. As a consequence, it represents a better cost-accuracy compromise for the numerical simulations of turbulent flows where the maximum time step is controlled by the lifetime of the smallest resolved turbulent structures. Numerical results for the well-documented high-pressure VKI LS-89 planar turbine cascade illustrate the potential of IRS4 for significantly reducing the overall cost of turbomachinery large eddy simulations, while preserving an accuracy similar to the explicit solver even for sensitive quantities like the heat transfer coefficient and the turbulent kinetic energy field.

1. Introduction

The design of modern turbomachinery components requires advanced computational fluid dynamics (CFD) tools. Turbomachinery flows are generally three-dimensional, unsteady, and often transitional. Additionally, they may be characterized by high Mach and Reynolds numbers, especially for compressor and high-pressure turbine configurations. Finally, they involve complex geometries and moving elements, with interactions between the fixed and moving wheels. Despite the intrinsic complexity of turbomachinery flows, CFD solvers are largely employed in the design process and are predominantly based on steady or unsteady Reynolds-averaged Navier–Stokes (RANS) models, due to their robustness and their moderate computational cost. However, RANS have known limitations in the prediction of non-equilibrium flows, and specifically flows with unsteadiness, separation, rotational effects, strong gradients and transition (see, e.g., [1]). High-fidelity, scale-resolving simulation approaches like direct numerical simulation (DNS) and large-eddy simulation (LES) have recently shown their potential for drastically improving the prediction of some crucial turbomachin-

ery flow features, like heat transfer and separation [2–10]. Unfortunately, DNS still remains prohibitively expensive or just unaffordable at moderate to high Reynolds numbers, like those occurring in high-pressure turbines and in compressor cascades. On the other hand, LES is still computationally too expensive to be feasible in the regular design cycle. Part of the problem is, once again, the relatively high Reynolds number of the flow over turbomachinery blades and the requirements for wall resolved LES of extremely fine meshes near the wall for capturing the energetic structures in the boundary layer. This is especially critical for LES solvers using explicit time integration schemes [3], since fine wall resolution leads to severe restrictions on the maximum allowable time step. The latter is much smaller than the time-step required to achieve a satisfactory accuracy level of the solution. A way of relaxing stability constraints consists in adopting an implicit time integration method. Unfortunately, this generally involves much larger computational and memory costs. As a consequence, fully implicit schemes are prohibitively expensive to use and some form of partial implicitation or approximate calculation of the Jacobians has to be used to reduce computational cost to an amenable level. Additionally, the accuracy of such implicit schemes is generally limited to second order (the most used approach being the second-order backward time discretization), which may introduce significant dissipation and dispersion errors if large time steps are used. On the

---

* Corresponding author.
  E-mail addresses: jean-christophe.hoarau@ensam.eu (J.-Ch. Hoarau), paola.cinnella@ensam.eu (P. Cinnella), xavier.gloerfelt@ensam.eu (X. Gloerfelt).

other hand, such large time steps are preferred to compensate the overcost associated with the resolution of a nonlinear implicit system of equations, including inner subiterations used to rule-out approximate linearization and factorization errors. Nonetheless, for wall-resolved LES and for DNS, the maximum allowable time step has in any case to be sufficiently small to resolve the life time of the tiniest structures in the simulations.

Inspection of the existing literature on LES and DNS applied to turbomachinery flows shows that the main time integrations strategies in use are explicit Runge–Kutta schemes (e.g. [6,7]) and second-order implicit schemes with dual time stepping or Newton-Raphson subiterations [6,11]. Sometimes hybrid approaches are adopted [3], whereby implicit schemes are used to relax the time step constraints in grid blocks close to the solid walls, whereas less costly explicit schemes are used to advance the calculation in grid blocks discretizing the blade passage.

In a recent work, a high-order accurate and efficient implicit scheme was proposed and applied to the LES and DNS of selected geometrically simple flow configurations, like homogeneous isotropic turbulence and turbulent channel flows [12]. The approach uses a high-order extension of the well-known Implicit Residual Smoothing (IRS) approach, initially proposed by Lerat et al. [13] and widely used in the past to speed-up convergence of steady Euler and Navier-Stokes calculations based on Runge–Kutta time stepping [14,15]. The high-order IRS uses an implicit bi-Laplacian smoothing operator (of fourth-order accuracy) to filter-out high-frequency modes of the residual, which leads to the solution of pentadiagonal systems for each space direction and Runge–Kutta stage. Thanks to the efficient inversion of scalar pentadiagonal matrices, the extra computational cost associated with the implicit operator was shown to remain much lower than standard implicit schemes at least for the considered configurations.

The present paper aims at assessing the benefits of the high-order IRS scheme for the LES of turbomachinery flows, both in terms of accuracy and computational cost. In order to deal with turbomachinery geometries, the scheme of Cinnella and Content [12] is generalized to multiblock curvilinear structured grids by using a finite-volume formulation. The proposed methodology is first validated on a simple flow case (vortex advection) and a 2D turbine rotor geometry, and subsequently applied to the LES of a high-pressure turbine cascade configuration, specifically, the VKI LS89 cascade. The latter has been extensively investigated both experimentally and numerically [3,4,6–9,16,17]. The sensitivity of the numerical results to the tuning parameters of the IRS scheme and the benefits compared to standard explicit Runge–Kutta and second-order implicit schemes are shown up.

The paper is organized as follows: Section 2 presents the governing equations and the time and space integration schemes used in this study. Section 3 reports preparatory validations for underlying flow configurations. LES results for the LS89 cascade are presented in Section 4. Finally, Section 5 contains concluding remarks and perspectives for future work.

2. Numerical methods

We consider the compressible Navier–Stokes equations in their instantaneous, Reynolds-averaged or filtered formulation. A finite volume (FV) approach is used to deal with non-Cartesian mesh geometries, so that the corresponding system of conservation laws is written in the integral form:

$$\frac{d}{dt}\int_{\Omega} w \, d\Omega + \oint_{\partial\Omega} \boldsymbol{\phi} \cdot \boldsymbol{n} \, d\Gamma = 0 \qquad (1)$$

with initial conditions

$$w(x, y, z, 0) = w_0(x, y, z)$$

where t is the time, x, y and z are Cartesian space coordinates, $w = [\rho, \rho U, \rho V, \rho W, \rho E]^T$ is the vector of conservative variables (with ρ the fluid density, U, V, W the Cartesian components of the velocity vector and E the specific total energy), Ω is a closed control volume with boundary $\partial\Omega$, $\boldsymbol{\phi}$ is the physical flux density and $\boldsymbol{n}$ is the unit outward normal. The flux density contains the contributions of both the convective and viscous fluxes: $\boldsymbol{\phi} = \boldsymbol{\phi}_c - \boldsymbol{\phi}_v$, where $\boldsymbol{\phi}_c$ and $\boldsymbol{\phi}_v$ are smooth functions of the variables (w), and of the variables and their spatial gradient (w, ∇w), respectively.

The viscous fluxes may be set to zero (for inviscid flows), or may contain the contributions of the Reynolds stresses (for RANS calculations) or the contributions of the subgrid stresses (for LES calculations). In practice, the LES presented in the following are conducted without the introduction of an explicit model for the subgrid terms, i.e. we carry out an Implicit LES (ILES, [18,19]), whereby the damping of unresolved subgrid scales is ensured implicitly by the regularizing numerical dissipation term associated with the spatial scheme, as discussed later.

2.1. Spatial discretization

Define a structured mesh composed of hexaedral cells $\Omega_{j,k,l}$ and denote the cell faces by $\Gamma_{j+\frac{1}{2},k,l}$, $\Gamma_{j,k+\frac{1}{2},l}$ or $\Gamma_{j,k,l+\frac{1}{2}}$, such that:

$$\partial\Omega_{j,k,l} = \Gamma_{j+\frac{1}{2},k,l} \cup \Gamma_{j,k+\frac{1}{2},l} \cup \Gamma_{j,k,l+\frac{1}{2}}$$
$$\cup \Gamma_{j-\frac{1}{2},k,l} \cup \Gamma_{j,k-\frac{1}{2},l} \cup \Gamma_{j,k,l-\frac{1}{2}}$$

The cell volume is denoted by $|\Omega_{j,k,l}|$ and an edge surface by $|\Gamma_{j+\frac{1}{2},k,l}|$. For each cell face $\Gamma_{j+\frac{1}{2},k,l}$, we denote $\boldsymbol{\Gamma}_{j+\frac{1}{2},k,l}$ the oriented surface directed in the sense of increasing mesh indices. For each cell $\Omega_{j,k,l}$ we identify the cell center, noted $C_{j,k,l}$, by its coordinates ($x_{j,k,l}$, $y_{j,k,l}$, $z_{j,k,l}$), and we denote its maximum dimension in each direction as $\delta x_{j,k,l}$, $\delta y_{j,k,l}$, and $\delta z_{j,k,l}$, respectively. In this work, we consider cell-centered finite volume schemes, i.e. we choose to locate the unknown vector w at cell centers. Finally, we define a characteristic mesh size by $h = \max(\max_{j,k,l} \delta x_{j,k,l}, \max_{j,k,l} \delta y_{j,k,l}, \max_{j,k,l} \delta z_{j,k,l})$.

Applied to the cell $\Omega_{j,k,l}$, the conservation law (1) reads:

$$\frac{d}{dt}\int_{\Omega_{j,k,l}} w \, d\Omega + \sum_{\Gamma\in\partial\Omega_{j,k,l}} \int_{\Gamma} \boldsymbol{\phi} \cdot \boldsymbol{n} \, d\Gamma = 0 \qquad (2)$$

By introducing suitable approximations of the volume and surface integrals, Eq. (2) can be written:

$$|\Omega_{j,k,l}|\frac{d}{dt}\left(\tilde{\mathcal{V}}w\right)_{j,k,l} + \tilde{\mathcal{S}}(w_{j,k,l}) = 0 \qquad (3)$$

where $\tilde{\mathcal{V}}$ is a (linear) operator approximating the volume integral

$$\left(\tilde{\mathcal{V}}w\right)_{j,k,l} = \frac{1}{|\Omega_{j,k,l}|}\int_{\Omega_{j,k,l}} w \, d\Omega + \mathcal{O}(h^p) \qquad (4)$$

and $\tilde{\mathcal{S}}$ approximates the surface integrals

$$\tilde{\mathcal{S}}(w_{j,k,l}) = \sum_{\Gamma\in\partial\Omega_{j,k,l}} \left(\int_{\Gamma} \boldsymbol{\phi} \cdot \boldsymbol{n} \, d\Gamma + |\Gamma|\mathcal{O}(h^p) \right) \qquad (5)$$

for any face Γ of $\Omega_{j,k,l}$. If Eqs. (4) and (5) are satisfied simultaneously, the FV approximation (3) is said to be accurate at order p in the FV sense [20].

In the present work, we use a five-point per direction spatial scheme [21] supplemented with nonlinear artificial dissipation based on a blending of second and fourth order derivatives [22]. Such a scheme is third-order accurate in smooth flow regions on sufficiently regular grids. Numerical dissipation throughout the domain is mostly ensured by the fourth derivatives, with

a dissipation coefficient (denoted k_4) that is kept as low as possible while ensuring robustness of the calculation. The lower-order nonlinear dissipation is used to damp unphysical oscillations in flow regions characterized by discontinuities, so that the corresponding coefficient (denoted k_2) may be set equal to zero for fully subsonic flows. An analysis of the spectral properties of the spatial discretization scheme for a linear scalar problem (not reported for brevity, see [23]), shows that, using $k_2 = 0$, $k_4 = 0.032$ the scheme requires a resolution of 10 and 16 points per wavelength to achieve, respectively, a dispersion and a dissipation error of 0.1% on a Fourier mode of the numerical solution at each timestep. Since the numerical scheme introduces already sufficient damping of the solution at smaller scales, and based on our previous studies [24,25], we choose an Implicit LES (ILES) modeling approach, which relies on the numerical viscosity for solution regularization.

2.2. Time integration schemes

In this section we first recall the baseline explicit time integration scheme, and then introduce the high-order implicit residual smoothing procedure. The formulation of the second-order backward implicit time integration scheme, used for comparison with the IRS in the following sections, is also described for completeness.

After approximating the space integrals by a suitable discretization scheme, Eq. (1) may be formally rewritten:

$$\left.\frac{dw}{dt}\right|_{j,k,l} + \frac{1}{|\Omega_{j,k,l}|}\mathcal{R}(w_{j,k,l}) = 0 \tag{6}$$

where $\mathcal{R}$ is the space approximation operator. The semi-discrete Eq. (6) represents a set of ordinary differential equations, depending on the number of degrees of freedom, control volumes or grid points contained in each grid.

2.2.1. Explicit Runge–Kutta scheme

The baseline explicit time integration scheme is the low-storage six-step optimized Runge–Kutta (RK6) method of Bogey and Bailly [26], widely used in the literature for LES and DNS calculation. This may be written in compact form as

$$\begin{cases} w_{j,k,l}^{(0)} = & w_{j,k,l}^{n} \\ \Delta w_{j,k,l}^{(k)} = & -a_k \frac{\Delta t}{|\Omega_{j,k,l}|}\mathcal{R}(w_{j,k,l}^{(k-1)}), k = 1, \dots s \\ w_{j,k,l}^{n+1} = & w_{j,k,l}^{(s)} \end{cases} \tag{7}$$

where w^n is the numerical solution at time $n\Delta t$, $\Delta w^{(k)} = w^{(k)} - w^{(0)}$ is the solution increment at the kth Runge–Kutta stage, $s = 6$ is the number of stages, and a_k are the optimized scheme coefficients. The latter can be found in [26]. The preceding RK6 is formally only second-order accurate but exhibits very low dispersion and dissipation errors up to the lowest resolved frequency for a given time-step Δt.

2.2.2. Implicit residual smoothing scheme

The stability domain of the explicit RK schemes can be enlarged by using an implicit residual smoothing (IRS) technique. The main idea of IRS is to run the explicit scheme with a time step greater than its stability limit. The calculation is then stabilized by smoothing the residual by means of a dissipative spatial operator added to the left hand side of Eq. (7). Most IRS operators introduced in the past were only first or second order accurate (e.g. [14,15]), and introduced large additional dissipation and dispersion errors with respect to the baseline time scheme. In this work we extend the stability domain of the baseline RK6 by means of a recently proposed high-order IRS scheme [12], presented hereafter in the finite-volume framework.

The IRS smooths the residuals by means of a bi-Laplacian increment at each Runge–Kutta stage. In compact form this writes:

$$\begin{cases} w_{j,k,l}^{(0)} = & w_{j,k,l}^{n} \\ \left(\prod_{d=j,k,l} \mathcal{J}_d\right)\Delta w_{j,k,l}^{(k)} = & -a_k \frac{\Delta t}{|\Omega_{j,k,l}|}\mathcal{R}(w_{j,k,l}^{(k-1)}), k = 1, \dots s \\ w_{j,k,l}^{n+1} = & w_{j,k,l}^{(s)} \end{cases} \tag{8}$$

In the preceding equation, $\mathcal{J}_d$ denotes the implicit residual smoothing operator in the dth direction. This is a conservative finite-volume extension of the finite-difference IRS operator of Ref. [12]. Specifically, for $d = j$, $\mathcal{J}_j$ is defined as:

$$\begin{aligned}\left(\mathcal{J}_j \Delta w\right)_{j,k,l} = & \Delta w_{j,k,l} + \theta \frac{\Delta t}{|\Omega_{j,k,l}|} \\ & \times \left[\sigma_{j+\frac{1}{2},k,l}^3 \lambda_{j+\frac{1}{2},k,l}^4 \left(\delta_j^3 \Delta w\right)_{j+\frac{1}{2},k,l} - \sigma_{j-\frac{1}{2},k,l}^3 \lambda_{j-\frac{1}{2},k,l}^4 \left(\delta_j^3 \Delta w\right)_{j-\frac{1}{2},k,l}\right]\end{aligned} \tag{9}$$

where we introduced the difference operator in the grid direction j

$$\delta_j(\bullet)_{j+\frac{1}{2},k,l} = (\bullet)_{j+1,k,l} - (\bullet)_{j,k,l}$$

such that, e.g.,

$$(\delta_j^3 \Delta w)_{j+\frac{1}{2},k,l} = \Delta w_{j+2,k,l} - 3\Delta w_{j+1,k,l} + 3\Delta w_{j,k,l} - \Delta w_{j-1,k,l}$$

The coefficient σ, defined at cell face $\Gamma_{j+\frac{1}{2},k,l}$ is given by

$$\sigma_{j+\frac{1}{2},k,l} = \frac{\Delta t}{|\Omega_{j+\frac{1}{2},k,l}|}$$

with $|\Omega_{j+\frac{1}{2},k,l}| = \left(|\Omega_{j+1,k,l}| + |\Omega_{j,k,l}|\right)/2$. Finally, θ is a tuning parameter and λ is the spectral radius (denoted $\rho(\bullet)$) of the inviscid flux Jacobian along the jth direction:

$$\lambda_{j+\frac{1}{2},k,l} = \rho\left(\left.\overline{\frac{d\boldsymbol{\phi}_c}{dw}}\right|_{j+\frac{1}{2},k,l} \cdot \boldsymbol{\Gamma}_{j+\frac{1}{2},k,l}\right)$$

where the interface value $\left.\overline{\frac{d\boldsymbol{\phi}_c}{dw}}\right|_{j+\frac{1}{2},k,l}$ is computed as an arithmetic average of the Jacobians at cell centers $C_{j,k,l}$ and $C_{j+1,k,l}$. Similar formulas and definitions hold for mesh directions k and l.

An analytical study of the optimum value of θ for unconditional stability is difficult, but a numerical search for a 1D scalar problem [12] shows that unconditional stability is obtained for:

$$\theta \gtrsim 0.005$$

For a 1D system of conservation laws and a regular Cartesian grid the additional error introduced by the IRS operator with respect to the explicit scheme is of the form:

$$-\frac{1}{12}\theta \Delta t^4 \rho(A)^4 \frac{\partial^5 \boldsymbol{\phi}_c}{\partial x^5} + O(\Delta t^4), \qquad A = \frac{d\boldsymbol{\phi}_c}{dw} \tag{10}$$

ie., the proposed IRS treatment introduces an additional error of $O(\Delta t^4)$, with respect to the baseline RK6. For this reason, this scheme is referred to as IRS4 in the following. Being proportional to a fifth derivative of the flux function $\boldsymbol{\phi}_c$, this error is recognized to have a dispersive nature. The error increases for larger values of the Courant–Friedrichs–Lewy (*CFL*) number and of the smoothing coefficient θ. As a consequence, the latter has to be taken as small as possible to ensure stability while not deteriorating accuracy. A detailed study of the dissipation and dispersion error introduced by the IRS4 scheme in the Fourier space has been carried out in [12], showing that the smoothing operator does not alter the accuracy of the baseline scheme in use significantly, provided that the *CFL* number is not too high (typically, below 10). Such findings were verified for a linear advection problem and for the DNS of

geometrically simple flow configurations, namely the decay of homogeneous isotropic turbulence and a turbulent channel flow. The aim of this work is to assess the validity of the above-mentioned theoretical results for more realistic and challenging configurations.

The factorized IRS4 operator $\mathcal{J}_d$ in Eqs. (8)-(9) leads to the inversion of a pentadiagonal matrix per mesh direction at each Runge–Kutta step. Such a matrix requires special treatment close to the borders of a mesh block. Different treatments are used for solid walls and for permeable boundaries (inlet, outlet, and interior boundaries between adjacent blocks for multi-block computations). When Dirichlet boundary conditions are applied, the solution increment at the boundary is set equal to 0. For other kinds of boundary conditions (*ie.* Neumann, mixed or periodic) and at interior boundaries, layers of ghost cells are used to make mesh blocks independent from each other and reduce the required number of parallel communications. A minimum of two layers of ghost cells is required by the present five-point IRS operator. Within the ghost cells, information for computing $\mathcal{J}_d$ is lacking, and the IRS operator is simply set equal to the identity, which means that the ghost cells are advanced explicitly in time, while the right-hand sides are communicated from the neighboring block. Such a procedure leads to the inversion of an $(n+2) \times (n+2)$ matrix in each mesh direction, n being the number of inner cells. This simplified treatment may however lead to stability problems for high values of the *CFL* (larger than 10). Besides, it introduces an additional error with respect to the single-block IRS operator, which may be reduced by using a redundant number of ghost cells. Increasing the number of ghost cells implies a computational overcost in terms of parallel communications among mesh blocks, which varies according to the spatial operator in use. The simulation presented in the following are based on a 5-point spatial discretization operator, which also requires two layers of ghost cells for multiple-block computations. Thus, if only two layers of ghost cells are used for the IRS treatment, the overcost associated with parallel communications to the ghost cells is rather small, and good parallel scalability is observed by using mesh blocks with at least 50^3 cells. However, a number of ghost cells larger than two may be required for preserving accuracy, and the final choice derives from a trade-off between computational cost and accuracy. The influence of the number of ghost cells involved in the IRS treatment on both accuracy and computational efficiency is investigated in the following Section.

2.2.3. Backward difference schemes

In order to assess the performance of the IRS4 scheme, a widely used second-order implicit scheme is also considered in some of the following simulations. Specifically, we consider the second-order backward multistep scheme (Gear scheme), which writes:

$$F_{j,k,l}^{n+1} = \frac{Dw_{j,k,l}^{n+1}}{\Delta t} + \frac{1}{|\Omega_{j,k,l}|} \mathcal{R}(w_{j,k,l}^{n+1}) = 0, \tag{11}$$

with

$$\frac{Dw_{j,k,l}^{n+1}}{\Delta t} = \frac{3\Delta w_{j,k,l}^{n} - \Delta w_{j,k,l}^{n-1}}{2\Delta t},$$

and $\Delta w^n = w^{n+1} - w^n$. Like all second-order schemes, the leading error term of Gear scheme is of dispersive nature.

Eq. (11) represents a system of non linear equations that is solved at each physical time step by means of the Newton-Raphson method. For this purpose, the residual is linearized, leading to:

$$\left. \frac{dF}{dw} \right|_{j,k,l}^{n} \Delta w_{j,k,l}^{n} = -F_{j,k,l}^{n}, \tag{12}$$

with the Jacobian:

$$\left. \frac{dF}{dw} \right|_{j,k,l}^{n} = \frac{3}{2\Delta t} I + \frac{1}{|\Omega_{j,k,l}|} \left. \frac{d\mathcal{R}}{dw} \right|_{j,k,l}^{n}$$

In practice, the Jacobian of the spatial operator is not computed exactly. As we use high-order schemes for the evaluation of the explicit part, the full implicitation could not be performed without a considerable computational cost per iteration. This difficulty is circumvented by applying a defect correction approach, in which a first-order Roe–Harten operator is used to approximate the Jacobian matrix. Finally, a Krylov subspace method, namely GMRES, is used to solve Eq. (12) iteratively using the approximate Jacobian. Due to the use of an iterative technique instead of a direct linear solver, the resulting algorithm is categorized as an "inexact" Newton method. The reader may refer to [27] for more details on the formulation of the implicit scheme.

The number of sub-iterations required to converge Eq. (12) depends on the problem and on the properties of the spatial discretization scheme. In the following calculations, the number of iterations of the inner loop is set equal to 4 and the inexact Newton iteration is converged until the residual is reduced by two order of magnitude with respect to the initial value or when a maximum number of inner iterations is reached. For instance, for the expensive LES of Section 4 the maximum number of inexact Newton subiterations was limited to 10.

3. Preliminary validations

In this section the accuracy and efficiency of the IRS4 are preliminarily assessed for two test cases preparatory to the turbine LES presented in Section 4. The first test case allows an investigation of the scheme implementation for multi-block grids. The second one is a preliminary application to the unsteady flow around a turbine cascade, computed at this stage by solving the unsteady RANS equations.

All the numerical methods described in Section 2 are implemented within the in-house structured finite-volume code DynHoLab [28].

3.1. Vortex advection

The IRS4 is used to simulate the advection of a Taylor vortex by an inviscid uniform field. This test case has been often used to investigate the accuracy of numerical methods for computational aeroacoustics and is very sensitive to the boundary treatment [29]. The Taylor vortex is defined by the following velocity and pressure fields:

$$\begin{cases} u = A\dfrac{y}{\Delta y} \exp(\alpha R^2) \\ v = v_\infty - A\dfrac{x}{\Delta x} \exp(\alpha R^2) \\ p = p_\infty - \rho_\infty \dfrac{A^2}{4\alpha \Delta x \Delta y} \exp(2\alpha R^2) \end{cases} \tag{13}$$

where $R = \sqrt{(x-x_0)^2 + (y-y_0)^2}$ with $(x_0, y_0) = (-12.5, 12.5)$ the initial vortex position, $\alpha = -\ln 2/b^2$ and where we chose the half-width $b = 10 \times \Delta x = 2.5$m and the vortex strength $A = 10$ m/s. The vortex is embedded in a constant mean flow with Mach number $M = v_\infty/c_\infty = -0.5$, i.e., it is advected downwards in the vertical direction. The vortex is set in a rectangular computational domain of sides $L_x = L_y = 50$m. The domain is discretized by a set of four uniform Cartesian grids with a number of cells varying between 100×100 and 1600×1600, subdivided into four equally sized blocks. The time-step used for the computations is reduced according to spatial mesh refinement, and varies between
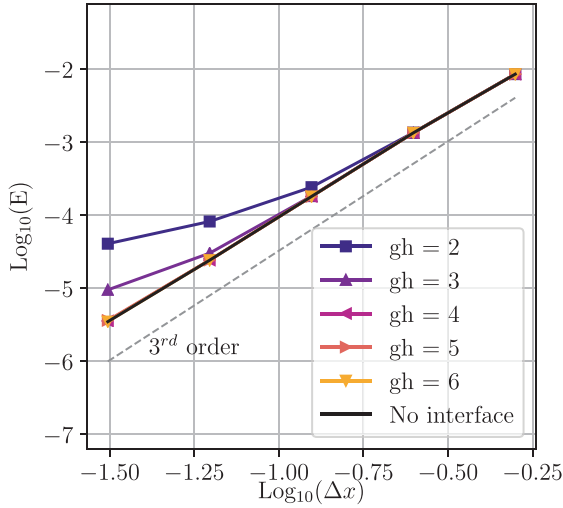
Fig. 1. Vortex advection problem: L_∞ norm of the error E with respect to the exact solution at final time, $CFL=2.5$, and various numbers of ghost cells, as a function of the mesh size Δx.

$\Delta t = 2.2 \times 10^{-3}$ and $\Delta t = 0.137 \times 10^{-3}$ s, respectively, corresponding to a maximum *CFL* number of about 2.5. During the advection, the vortex crosses the subdomain border, located at $y = 0$. Several computations are carried out by varying the number of ghost cells (*gh*), and the results are compared to those obtained using a single mesh block. For all the computations, the smoothing coefficient is $\theta = 0.01$ and the artificial dissipation coefficients of the spatial scheme are $k_2 = 0.$ and $k_4 = 0.032$.

Fig. 1 shows the L_∞ norm of the error with respect to the exact solution, corresponding to pure advection of the initial vortex at constant velocity. Firstly, we notice that a convergence order of about three is obtained for the single-block computation, which is higher than the order of the present time integration scheme and close to the order of the spatial scheme, showing that the time error is much smaller than the spatial error. The simplified IRS treatment at inter-block boundaries reduces the convergence order if only two layers of ghost cells are used. Increasing the number of ghost cells allows restoring the original accuracy and, for $gh = 4$ or higher, the solution is superposed to the single-block one.

In Fig. 2 we report the iso-contours of the fluctuating pressure field (on the grid 200×200) by using an increasing number of ghost cells. A higher maximum *CFL* number (equal to 5) is used here, to emphasize the differences among the various cases. In the same figure, we also report the results obtained with the second-order implicit Gear scheme and the same maximum *CFL*, as well as the exact solution. Increasing the number of ghost-cells from $gh = 2$ to $gh = 5$ decreases the spurious noise generated when crossing the internal border. Thanks to the inner subiterations, the Gear scheme generates lower errors at the interface using only two layers of ghost cells (as required by the spatial scheme). However, it introduces significant dispersion and dissipation errors at inner mesh points, leading to considerable deformation and smearing of the transported vortex. The L_∞ errors for an increasing number of ghost cells are plotted in Fig. 3 for the grid 200×200 and three values of the *CFL* number. It is worth noting that the effect of the ghost cells on the error becomes significant as the *CFL* number is increased up to 10.

For this simple 2D problem we did not observe any appreciable impact of the number of ghost cells in use on the computational cost of the IRS4 scheme (differences of the order of 7% between $gh = 2$ and $gh = 6$). In all cases the IRS calculations allow reducing the overall CPU cost by a factor larger than 2 with respect to the Gear scheme.

3.2. Turbine cascade VKI LS-59

For preliminary assessment of the IRS scheme on a more challenging flow configuration, and in view of the LES of a turbine flow, the IRS4 is then applied to a 2D unsteady flow in a turbine cascade. More specifically, we chose the VKI LS-59 transonic turbine rotor cascade, previously considered in several experimental and numerical studies [30–34]. To allow comparisons with other results in the literature, the flow is modeled through the unsteady RANS equations, supplemented by the Wilcox $k - \omega$ [1] model of turbulence. The VKI LS-59 is a high-loaded rotor blade with a thick, rounded trailing edge originally designed for near-sonic exit flow conditions. This rotor blade has been extensively tested in various European wind tunnels [30]. Experiments are available in a wide range of conditions, and Schlieren photographs clearly indicate the existence of vortex shedding downstream of the blade trailing edge, which is responsible for an appreciable fraction of profile losses. The flow conditions considered for this study correspond to an outlet isentropic Mach number equal to 1 and to a Reynolds number (based on the chord and exit conditions) of 7.44×10^5. The inlet angle is $30°$. This choice is motivated by the fact that most numerical computations available in the literature have been made for these conditions, and experimental distributions of the isentropic Mach number at the wall are also available for closeby conditions. Indeed, the configuration is affected by both geometrical and operational uncertainties, since the blade geometries used in the various tests reported in [30] exhibit slight differences that affect the shock location and intensity, and the outlet isentropic Mach and Reynolds number also exhibit small differences in the various tests. The computational domain, constituted of a single blade passage, is discretized by a single-block C-grid of 384×32 cells, with a first cell height leading to $\Delta y^+ \approx 2$. Non reflective boundary conditions are applied at the inlet and outlet boundaries, and periodic conditions are imposed at the lower and upper boundaries of the domain. The unsteady simulations are initialized with a (partially converged) steady RANS field obtained using the implicit backward Euler scheme available in the DynHoLab code [27] and a local time step.

All the results presented in this Section were obtained by applying the third-order spatial scheme with artificial dissipation coefficients $k_2 = 0.5$ and $k_4 = 0.032$. The IRS4 was applied using $\theta = 0.01$ as smoothing parameter and a constant time step leading to a maximum $CFL \approx 7$, which corresponds to approximately 5000 time-steps per vortex shedding period. For the present single-block grid, the effect of the number of ghost cells is restricted to the treatment of the connection line behind the trailing edge. Numerical tests conducted by varying the number of ghost cells did not reveal any significant influence on the accuracy and computational cost of the simulations. As a consequence only the results corresponding to $gh = 2$ are reported in the following of this section.

For this slow unsteady flow problem (only the mean flow instability in the wake is captured by the unsteady RANS solver), the explicit RK scheme leads to very severe constraints on the maximum allowable time step, and was discarded. For comparison with the IRS4, we carried out two simulations using the Gear scheme. For the first simulation, we use the same physical time step as in the IRS case. In such conditions, 6 to 10 subiterations are needed to satisfy the prescribed tolerance on the residual. The second one uses a time step ten times larger (i.e. $CFL_{max} \approx 70$ and about 500 time steps per period). In this case, approximately 20 subiterations per time step are necessary to converge the inner loop. In all cases, the simulations were run over an integration time corresponding to 20 shedding periods.

In Fig. 4, snapshots of the density gradient corresponding to the three simulations described previously are compared to a Schlieren picture obtained experimentally by Kiock et al. [30] (correspond-
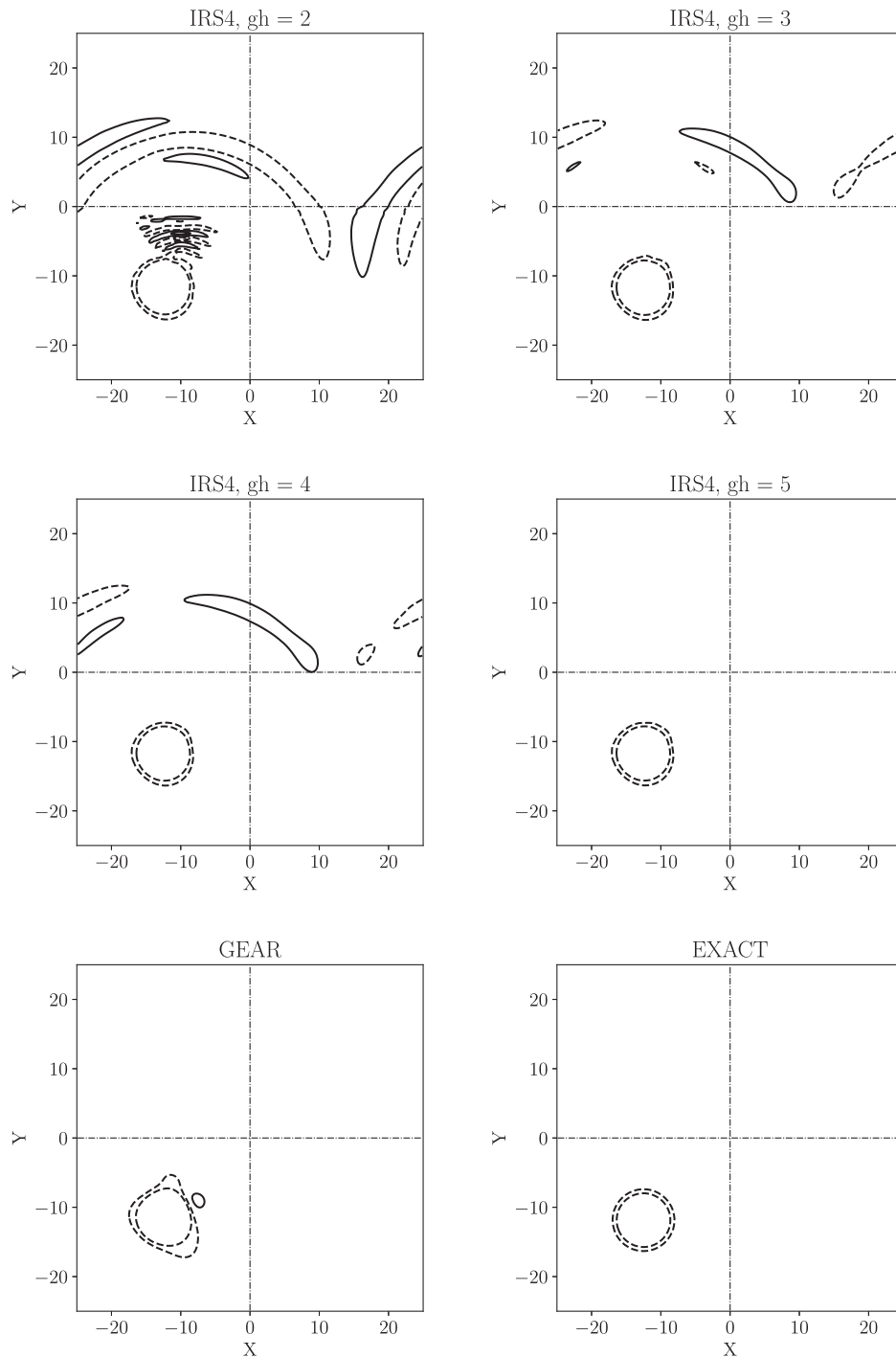
Fig. 2. Vortex advection problem: Isocontours of the fluctuating pressure (Δp=100 Pa, min = -150 Pa, max = 150 Pa) on the grid 200 $\times$ 200 and *CFL*=5. Positive and negative values are represented with solid and dashed lines, respectively.

ing to slightly different exit conditions). The flow is characterized by shock waves departing from the blade trailing edge and by vortex shedding in the wake. In all cases, an instability of the wake is observed. However, the simulation based on the Gear scheme and 500 time steps per period does not resolve accurately the vortices shed in the wake. Fig. 5 shows the distribution of the isentropic Mach number along the blade, averaged over 10 shedding periods. The present results are compared to two series of experimental data from Kiock et al. [30] and to the numerical results of Michel et al. [34] (based on the Spalart-Allmaras turbulence model and using a Residual-Based-Compact scheme for the spatial discretiza-

tion and a second-order implicit time discretization). This quantity of interest is little affected by the time integration scheme, and all the results are in good agreement with the numerical data and match reasonably well the experimental measurements. The largest differences are observed at the upper side in the vicinity of $x/c = 0.6$, which corresponds to the reflection of the impinging shock and is a particularly sensitive zone. Fig. 6 shows the Fourier transform of the time-dependent tangential force acting on the blade. A well-defined peak corresponds to the shedding frequency. The corresponding Strouhal number (based on the trailing edge thickness and exit velocity) is about 0.21 for the computations
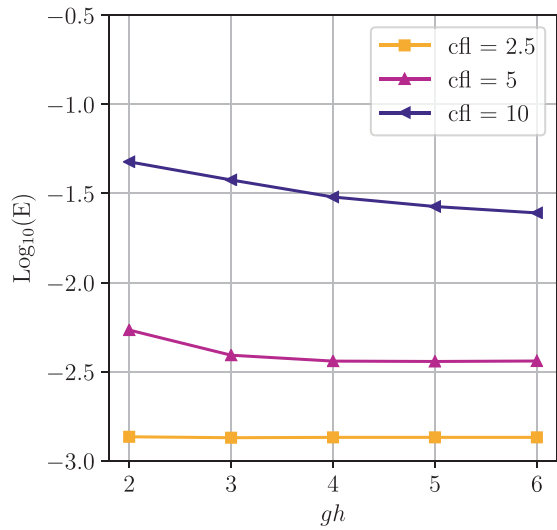
Fig. 3. L_∞ norm of the error E as a function of the number of ghost cells gh on the grid 200×200.
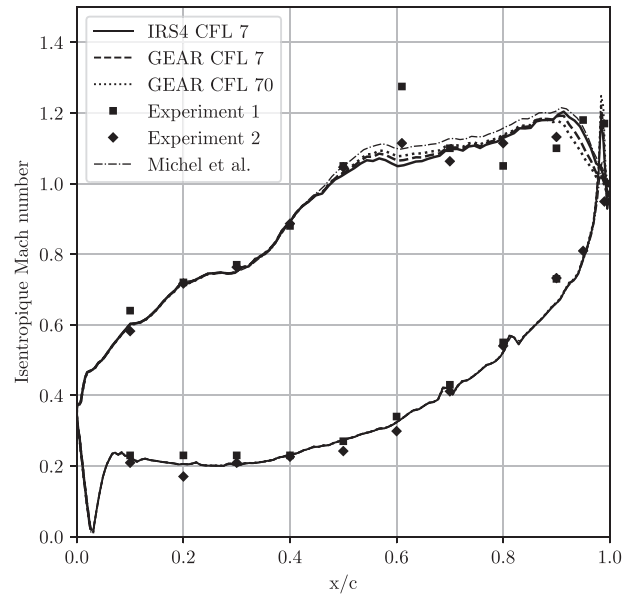

Fig. 5. VKI LS-59 cascade: time-averaged wall distribution of the isentropic Mach number for various time integration schemes. Comparison with experimental [30] and numerical results [34].
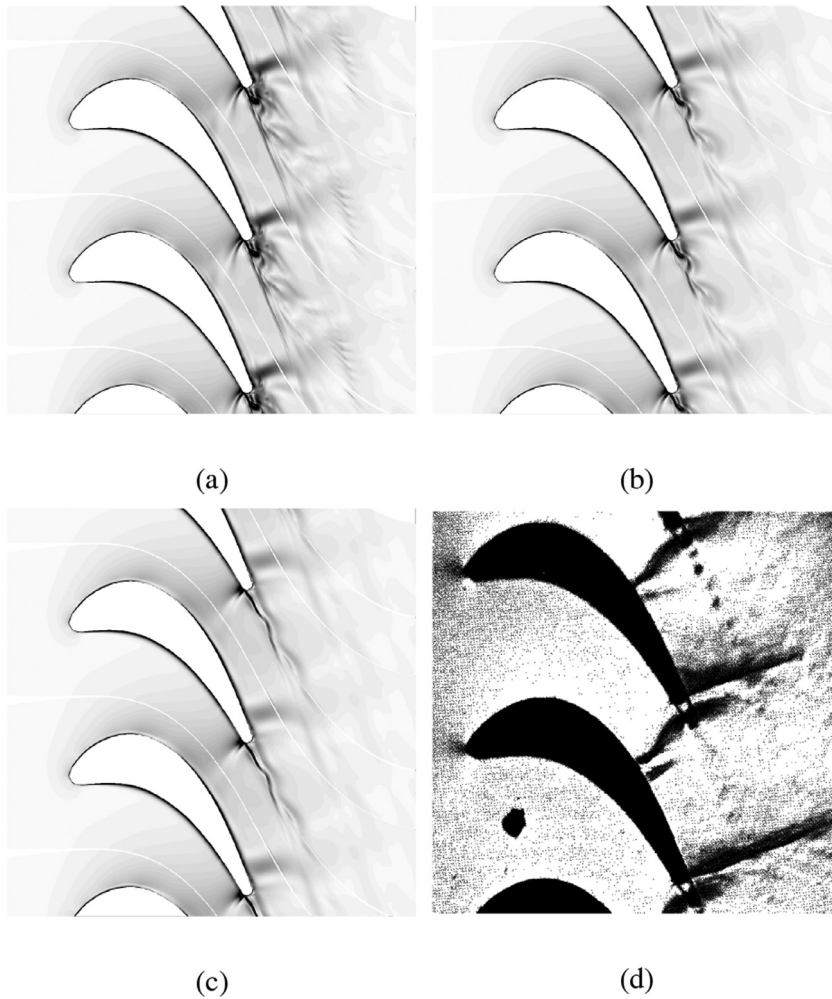

(a)

(b)

(c)

(d)

Fig. 4. VKI LS-59 cascade: snapshots of the density gradient computed with the IRS4 scheme at $CFL_{max} \approx 7$ (a), and with the Gear scheme at $CFL_{max} \approx 7$ (b), and $CFL_{max} \approx 70$ (c); Schlieren picture from Kiock et al. [30] (d).

Fig. 6. VKI LS-59 cascade: Fourier spectra of the tangential force on the blade for various time integration schemes, as a function of the Strouhal number.

Table 1
VKI LS-59 cascade: CPU cost [s] for various time integration scheme. The cost corresponds to the time integration over two vortex shedding cycles. The computational costs were measured on an IBM x3750M4 supercomputer (Intel Sandy Bridge Processors). Single-processor calculation.

Scheme	IRS4	GEAR *CFL* 7	GEAR *CFL* 70
Number of iterations	10,000	10,000	1000
CPU Time (s)	10,260	15,582	4190
CPU cost per iteration	1.026	1.558	4.19

with the smallest time step, and about 0.20 for the computation with $CFL_{max} \approx 70$. In all cases, the latter is in good agreement with previous numerical results, e.g. [34], and in reasonable agreement with the range of frequency [0.2,0.4] observed experimentally for a similar cascade configuration [35], although the larger numerical errors introduced by the second-order implicit time scheme with a large time step lead to a slightly lower value.

With the present setting, the cost per physical time step and per mesh cell of the IRS4 coupled with RK6 is 1.2 times lower than the cost of the Gear scheme with the same CFL_{max}, see Table 1. When the CFL_{max} is increased, the computational cost per iteration of the second-order scheme is nearly 3 times larger than the IRS. In this case, however, a much larger time step is allowed (although with some loss of accuracy) and thus the overall CPU cost is lower. This is an expected result, since the second-order explicit scheme with Newton-Raphson subiterations is particularly well suited to slow unsteady problems.

4. Large-eddy simulation of the VKI LS-89 turbine cascade

In this section, the IRS4 scheme is applied to the LES of the flow around the VKI LS-89 planar turbine cascade instrumented at the von Kármán Institute by Arts et al. [16]. The chord blade C is 67.647 mm long with a pitch-to-chord ratio of 0.85 and a stagger angle $\chi = 55°$. The flow angle at turbine inlet is equal to $0°$. For this configuration, several sets of experimental data are available, characterized by various inlet turbulent intensities and
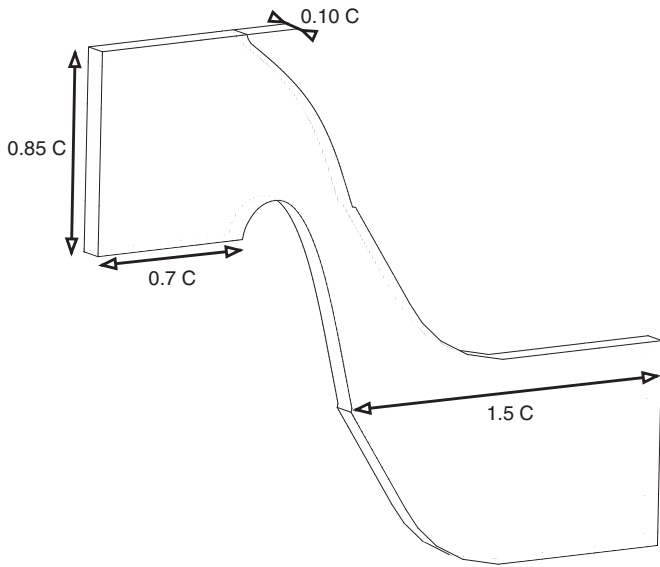
pressure ratios. Hereafter, we select flow conditions corresponding to the experiment called MUR129. This corresponds to an inlet total pressure $P_0 = 1.87 \times 10^5 Pa$, outlet isentropic Mach number $M_{is,2} = 0.840$ and outlet Reynolds number $Re_2 = 10^6$. An isothermal wall condition is used, with wall temperature $T_w = 298K$. In this experiment, the inlet free-stream turbulence intensity is very low, $Tu = 1\%$. Since our main goal is to assess numerical methods rather than to closely reproduce the experimental configuration, no inlet turbulence was prescribed in the present numerical simulations. This has the advantage of simplifying the numerical setup and reducing the number of parameters susceptible to affect the computed solutions. For the computed conditions, the flow field is subsonic, and natural boundary layer transition occurs at the rear of the blade upper surface.

The computational domain used for the present LES is displayed in Fig. 7(a). The mesh is a H-type structured mesh composed of 850 cells in the streamwise direction, 180 in the pitchwise direction and 200 in the spanwise direction. The total number of cells for the blade passage is equal to 30.6×10^6. The blade upper and lower surfaces are discretized by 550 cells each. A close-up view of the computational mesh (every four points are represented) is provided in Fig. 7(b). The corresponding distributions of Δy^+, Δx^+ and Δz^+ are shown in Fig. 8. The friction velocity, used for computing the wall coordinates, is based on the local values of the wall shear stress. The average first layer size is 2.5 μm, corresponding to $\Delta y^+ \approx 2$. The average resolutions in the streamwise and spanwise directions are $\Delta x^+ \approx 100$ and $\Delta z^+ \approx 25$. These values correspond to a coarse LES, but are similar to those of Collado et al. [6]. The LES is initialized with a preliminary 2D laminar calculation extruded in the spanwise direction. A sinusoidal perturbation of the conservative variables with an amplitude of 10% is applied in the spanwise direction only on the initial solution, to speed-up the initial transient toward a fully 3D field. The simulations are first run over about ten flow-through times to evacuate the initial transient. A flow-through time is calculated as the time required for a particle dropped at the blade leading edge to reach the trailing edge, when traveling at a constant velocity approximated as the arithmetic average of the velocity at the passage inlet ($x = 0$ in our reference frame with origin at the blade leading edge) and the velocity at the passage outlet ($x = C \cos \chi$). Afterwards, the statistics are collected over the five subsequent flow-through times.
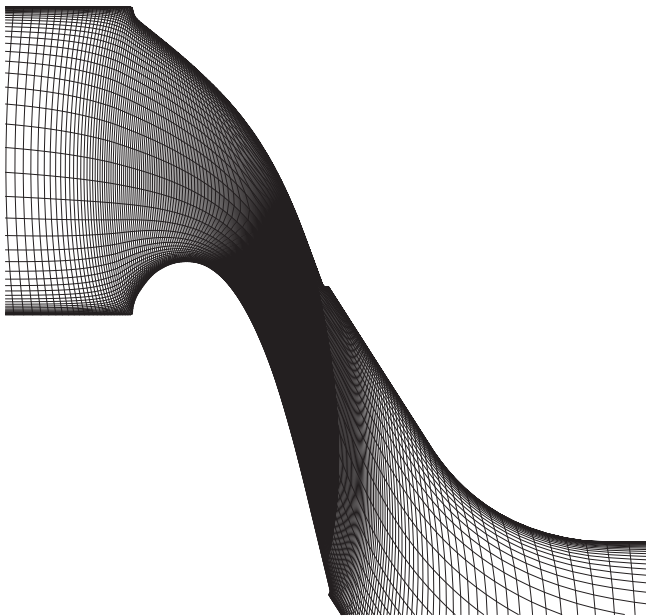
The artificial dissipation coefficients of the spatial scheme were taken equal to $k_2 = 0.$ and $k_4 = 0.064$ for this series of calculations.

For simulations based on the IRS4 time scheme, the dimensional time-step is set equal to 3×10^{-8} seconds, which corresponds to a maximum CFL number of approximately 7. The value of the smoothing parameter is set to $\theta = 0.01$ and two layers of ghost cells are used. The results are compared to those of the explicit scheme and the second-order implicit scheme. Due to the high computational cost of the simulation, the latter was carried out with a maximum number of Newton subiterations equal to 10.

Fig. 9 presents a typical field of the time-averaged Mach number, obtained with the IRS4 scheme. The flow field is smooth and subsonic everywhere. An overview of the instantaneous flow field is given in Fig. 10, showing an iso-surface of the Q-criterion ($Q = 10^3$) colored by the velocity magnitude (the domain spanwise length was reproduced three times for an easier visualization), as well as the distribution of the density gradient in the background plane. A close-up view on the trailing edge is displayed in Fig. 10(b). Although the average flow is subsonic, instantaneous weak shocks are observed in the trailing edge region. It is also possible to observe the instability growth and transition in the boundary layer at the suction side, with the formation of structures reminiscent of hairpins, and the onset of turbulence. Finally, the wake is characterized by coherent vortex sheddings. Note that, starting from a distance of about 1/3 of the blade chord from the trailing
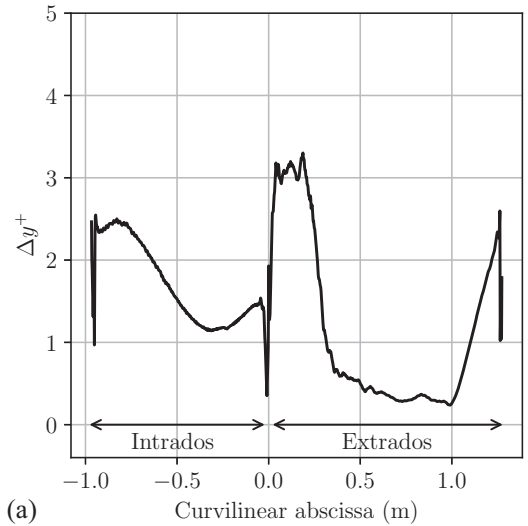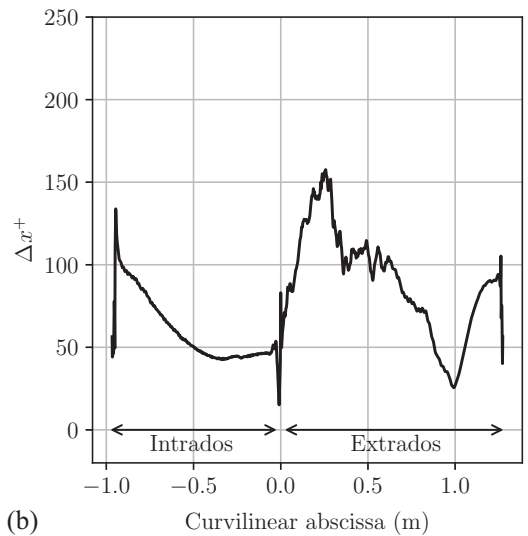
(a)

Fig. 7. Computational domain for the LES of the LS-89 cascade (a) and close-up view of the grid (b) (every four points are represented).

Fig. 8. VKI LS-89 cascade: Time- and span-averaged distributions of Δy^+ (a), Δx^+ (b) and Δz^+ (c) along the blade wall.

edge, the mesh does no longer provide a sufficient resolution of the turbulent structures in the wake. However, this has little influence on the prediction of the flow close to the blade wall. Flow snapshots for the RK6 and Gear schemes are qualitatively similar and are not reported.

Fig. 11 (a) provides the time averaged wall distribution of the isentropic Mach number, calculated with various schemes (IRS4, RK6, and Gear). The time step selected for the RK6 simulation corresponds to a maximum *CFL* of about 1, whereas for the Gear scheme we used the same time step as for the IRS4 computation. This quantity is weakly sensitive to the time integration scheme

Fig. 9. VKI LS-89 cascade: time-averaged isocontours of the Mach number (IRS4).

(a)

(b)

Fig. 10. VKI LS-89 cascade: iso-contour of the Q-criterion ($Q = 10^3$) colored with the velocity norm (a) and close up view near the trailing edge (b).

and all the results are in excellent accordance with the computation of Collado et al. [6], corresponding to the same flow conditions and using a computational grid with a similar resolution to the one used in the present computations. The weak influence of the time scheme shows that spatial resolution is more influential than time accuracy for this case. Since no experimental isentropic Mach number data are available for case MUR129, we consider experimental results [16] for slightly different flow conditions (MUR43), characterized by the same inlet turbulence intensity and outlet Mach and Reynolds numbers as MUR129, but a different total inlet pressure $P_0 = 1.435 \times 10^5 Pa$.
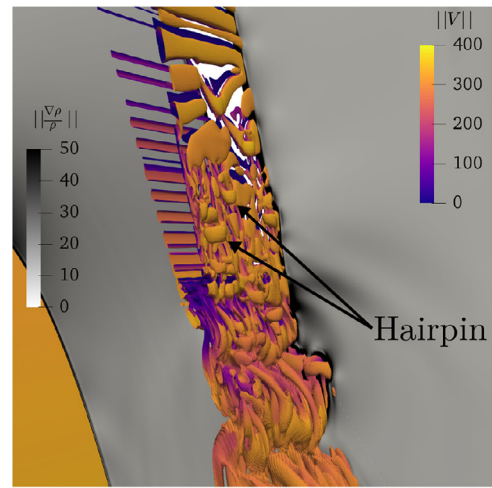
In figure 11(b), we report the time-averaged convective heat transfer coefficient at the wall, defined as:

$$H = \frac{q_w}{T_0 - T_w} \quad (14)$$

where q_w is the time-averaged wall heat flux, T_0 the total free stream temperature and T_w the wall temperature. The results obtained with various time schemes are compared to the experimental data of Arts et al. [16] for case MUR129 and to the numerical results of Collado et al. [6] and Segui et al. [9]. The solution of Collado et al. [6] was obtained by using a spatial scheme similar to the present one and a H–O–H grid with a resolution similar to the one considered in this study; time integration was carried out using a second-order dual time stepping method and the time step corresponds to a *CFL* of about 25. The solution of Segui et al. [9] is based instead on a third-order accurate explicit finite element solver and a hybrid unstructured grid of about 60×10^6 elements. The grid was adapted to obtain a very fine near wall spacing of about 5, 6 and 6 wall units in the wall-normal, streamwise and spanwise directions, respectively. Several considerations are in order. First, despite the rather coarse grid resolution, all the present simulations compare fairly to the experimental and numerical data from the literature. Specifically, the present LES captures reasonably well the increase of H at the upper surface blade near a curvilinear abscissa of 0.07, which is due to the boundary layer transition. On the other hand, the present coarse simulations tend to underestimate H in the middle of the upper surface and in the rear part of the lower surface. This may be due to the coarse grid resolution in such re-
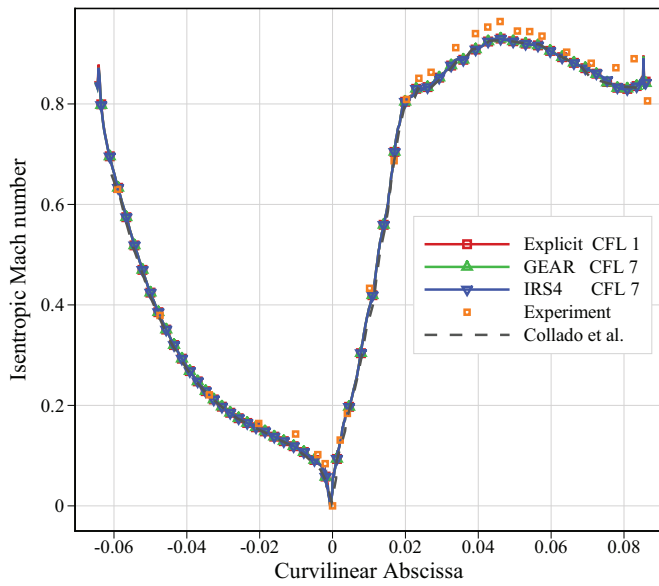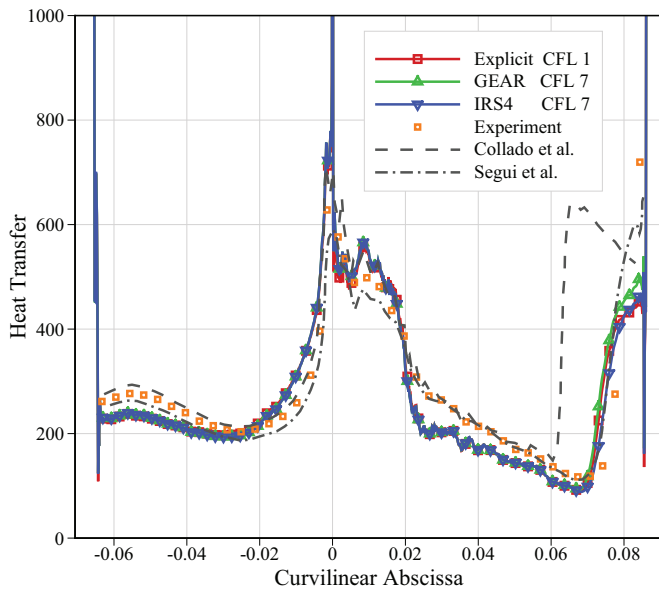
gion, characterized by an extremely fine boundary layer. Also note that the reference experiments and simulations use a non-zero turbulence intensity at the inlet. Second, all the time schemes in use provide similar results, except for minor differences in the transition region at the suction side. In particular, the IRS4 provides a solution in close agreement with the explicit scheme by using a time step seven times larger.

A sensitivity study to the IRS parameter θ and the number of ghost cells gh shows that the solution is essentially independent of the choice of these parameters (see Fig. 12). This indicates once again that the solution quality is dominated by spatial resolution for this case. Furthermore, due to mesh clustering, high values of the *CFL* number are reached only in the close vicinity of the wall, and the local *CFL* is close to unity elsewhere, reducing the influence of IRS on the solution accuracy.

For further investigation of the effect of time integration errors, a comparison of the resolved turbulent kinetic energy fields is reported in Fig. 13. This quantity depends on the resolved velocity fluctuations and is thus more sensitive to numerical errors than mean flow quantities. Both the IRS4 and Gear schemes provide iso-contours of the kinetic energy in excellent agreement with the reference explicit solution, showing that turbulent structures are well resolved in time.
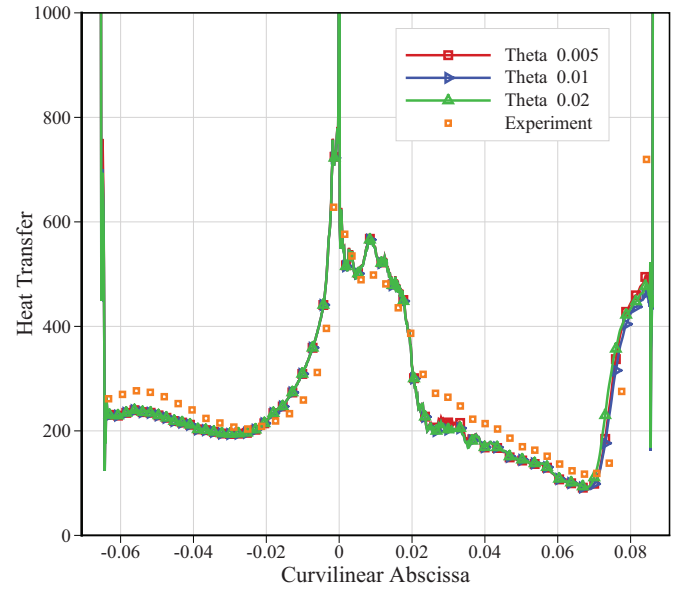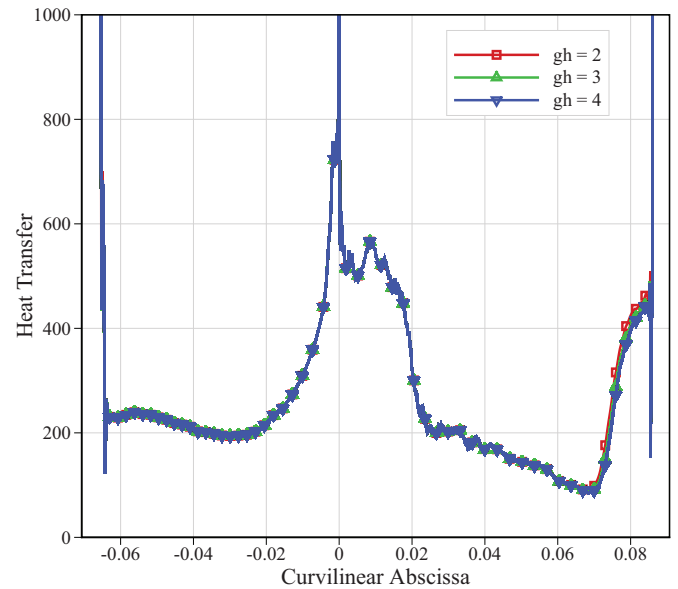
(a)

(b)

Fig. 11. VKI LS-89 cascade: time-averaged and span-wise averaged wall distributions of the isentropic Mach number (a) and of the convective heat transfer coefficient (b). Various time integration schemes.

(a)

(b)

Fig. 12. LS-89 cascade: sensitivity of the heat transfer coefficient to the IRS parameter θ (a) and the number of ghost cells gh (b).

We conclude this section with some considerations about the computational cost of the simulations. In Table 2 we report the overall CPU time corresponding to the calculation of flow statistics (five flow-though times) for various time schemes and numbers of ghost cells. Due to the severe constraints on the maximum allowable time step, the RK6 requires about one order of magnitude more time steps to cover the integration time interval. The IRS4 scheme, on the other hand, allows increasing the time step (while preserving a comparable accuracy) and has a computational cost per iteration only 35% higher if two layers of ghost cells are used. As a consequence, the overall CPU time is reduced by more than a factor 5 with respect to the explicit computation. This represents an extremely substantial improvement for costly LES. The computational gain is lesser if the number of ghost cells is increased. However, even when using 4 ghost cells, the overall

Table 2
LES of the VKI LS-89 cascade: computational cost for various time integration scheme. The cost is evaluated for the time interval corresponding to the computation of flow statistics (five flow-through times). The computational costs were measured on an IBM x3750M4 supercomputer (Intel Sandy Bridge Processors) and 250 processors were used in all cases.

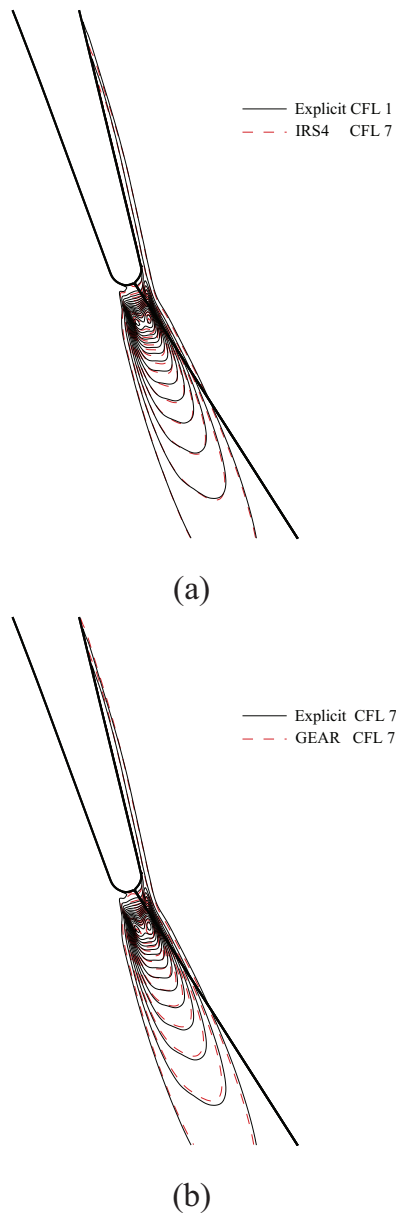| Scheme	gh	Number of iterations	CPU time/Processor (s)	Time per iteration and processor
RK6	2	450,000	933,750	2.075
IRS4	2	60,000	168,000	2.800
IRS4	3	60,000	219,000	3.651
IRS4	4	60,000	245,160	4.086
GEAR	2	60,000	348,600	5.810

(a)

(b)

Fig. 13. VKI LS-89 cascade: close-up view of the turbulent kinetic energy isocontours in the trailing edge region for various time integration schemes.

computational cost is almost four times lower than the explicit scheme. These costs are given for the present calculations using 250 blocks of approximately 49^3 points and may be dependent on the level of parallelization. The CPU cost for the Gear scheme is $1.5 \div 2$ times greater than IRS4 (depending on the number of ghost cells used), although it still represents a considerable improvement (about a factor 3) with respect to RK6.

The preceding results show the interest of using time implicit schemes for the LES of turbomachinery flows, the IRS4 scheme providing the best compromise between cost and accuracy. The computational gain is only weakly dependent on the number of ghost cells in use, which, on the other hand, have no significant influence on the solution accuracy for the present case.

5. Conclusions

A high order implicit time integration scheme based on the combination of a high-accurate implicit residual smoothing operator with an optimized Runge–Kutta scheme was extended to struc-

tured curvilinear grids by means of a finite volume formulation and applied to the numerical simulation of unsteady flows in turbomachinery, the focus being put on large eddy simulations of turbulent flows through turbine blade cascades. The proposed approach, called IRS4, is designed to enlarge the stability domain of the underlying Runge–Kutta scheme significantly without incurring in costly matrix inversions and Newton-Raphson subiterations and while preserving an accuracy similar to the explicit scheme over a range of *CFL* numbers $\lesssim 10$. The IRS4 scheme requires the inversion of a scalar pentadiagonal matrix per mesh direction, which can be done very efficiently. The scheme is parallelized by introducing layers of ghost cells at the interface between neighboring mesh blocks and by simplifying the smoothing operators at block borders, with a minimum of 2 layers. Numerical tests for a vortex advection problem show that very low error levels can be achieved by using 4 to 5 ghost cells instead of two.

Preliminary validations of the scheme were carried out for the simulation of transonic turbine rotor cascade, namely, the VKI LS-59 cascade, by solving the unsteady RANS equations. The flow is characterized by a mean flow instability in the wake region leading to the formation of a von Kármán vortex street. Although the IRS4 is not especially tailored for capturing this kind of low-frequency phenomenon, the overall computational cost is of the same order of that of a second-order implicit scheme (Gear scheme) with a time step ten times larger. This is due to the cost of the inner Newton subiterations used to solve the fully implicit scheme at each physical time step.

Finally, the IRS4 was applied to the LES of the high-pressure LS-89 turbine cascade. The simulations could be carried out using a maximum *CFL* of approximately 7 (i.e. about 7 times larger than the explicit scheme) and a comparable accuracy to the underlying explicit scheme. This leads to a reduction of the computational cost by a factor 5 for the same accuracy, using two layers of ghost cells. This factor reduces to about 4 when the number of ghost cell layers is increased to four. Note that, for the present computations, the solution was found to be little sensitive to the parameters chosen for the IRS4 scheme and dominated by the spatial resolution. Specifically, varying the number of ghost cell layers did not affect the results. The IRS4 solution was also compared to that obtained using the Gear scheme and the same maximum *CFL*. No appreciable differences between the numerical solutions are observed. However, the Gear scheme is about 1.7 times more costly than the IRS4, although it still allows a gain of a factor 3 with respect to the explicit scheme. In all cases, the present numerical results were found to compare fairly with experimental and numerical data from the literature, despite the use of a rather coarse grid.

In conclusion, the IRS4 was successfully extended and assessed for complex turbulent flows in turbomachinery configurations and was demonstrated to be a promising numerical technique to speed-up large eddy simulations of complex wall bounded flows.

References

[1] Wilcox D. Turbulence modeling for CFD. DCW Industries, Incorporated; 2006.
[2] Michelassi V, Wissink JG, Rodi W. Direct numerical simulation, large eddy simulation and unsteady Reynolds-averaged Navier–Stokes simulations of periodic unsteady flow in a low-pressure turbine cascade: a comparison. Proc Inst MechEng Part A 2003;217(4):403–11.
[3] Bhaskaran R, Lele S. Large eddy simulation of free-stream turbulence effects on heat transfer to a high-pressure turbine cascade. J Turbul 2010;11(6).

[4] Bhaskaran R, Lele S. Heat transfer prediction in high pressure turbine cascade with free-stream turbulence using LES. AIAA Paper, 2011–3266; 2011.

[5] Gourdain N, Gicquel L, Collado E. RANS and LES for the heat transfer prediction in turbine guide vane. J Propul Power 2012;28:423–33.

[6] Collado E, Gourdain N, Duchaine F, Gicquel L. Effects of free-stream turbulence on high pressure turbine blade heat transfer predicted by structured and unstructured LES. Int J Heat Mass Transf 2012;55(21):5754–68.

[7] Pichler R, Kopriva J, Laskowski G, Michelassi V, Sandberg R. Highly resolved LES of a linear HPT vane cascade using structured and unstructured codes. In: ASME Turbo expo conference, GT2016-49712; 2016.

[8] Wheeler A, Sandberg R, Sandham N, Pichler R, Michelassi V, Laskowski G. Direct numerical simulations of a high-pressure turbine vane. Journal of Turbomachinery 2016;138(7). 071003–9

[9] Segui L, Gicquel L, Duchaine F, de Laborderie J. LES of the LS89 cascade: influence of inflow turbulence on the flow predictions. In: European conference on turbomachinery fluid dynamics & thermodynamics; 2017.

[10] Pogorelov A, Meinke M, Schröder W. Large-eddy simulation of the unsteady full 3D rim seal flow in a one-stage axial-flow turbine. Flow Turbul Combust 2019;102(1):189–220.

[11] Marty J, Lantos N, Michel B, Bonneau V. LES and hybrid RANS/LES simulations of turbomachinery flows using high-order methods. In: ASME turbo expo conference, GT2015-42134; 2015.

[12] Cinnella P, Content C. High-order implicit residual smoothing time scheme for direct and large eddy simulations of compressible flows. J Comput Phys 2016;326:1–29.

[13] Lerat A, Sidès J, Daru V. An implicit finite-volume method for solving the Euler equations. In: Lecture Notes in Physics, vol. 170; 1982. p. 343–9.

[14] Jameson A, Baker T. Solution of the Euler equations for complex configurations. AIAA Paper, 83–1929; 1983.

[15] Blazek J, Kroll N, Rossow C-C. A comparison of several implicit residual smoothing methods. In: ICFD Conference on numerical methods for fluid dynamics; 1992.

[16] Arts T, Lambert de Rouvroit M, Rutherford A. Aero-thermal investigation of a highly loaded transonic linear turbine guide vane cascade: a test case for inviscid and viscous flow computations. VKI Training center for experimental aerodynamics technical note 174; 1990.

[17] Gourdain N, Gicquel L, Fransen R, Collado E, Arts T. Application of RANS and LES to the prediction of flows in high pressure turbine components. In: ASME Turbo expo conference, GT2011-46518; 2011. p. 1773–85.

[18] Rizzetta DP, Visbal MR, Blaisdell GA. A time-implicit high-order compact differencing and filtering scheme for large-eddy simulation. Int J Numer Methods Fluids 2003;42(6):665–93.

[19] Implicit large eddy simulation: computing turbulent fluid dynamics. Grinstein F, Margolin L, Rider W, editors. Cambridge University Press; 2007. doi:10.1017/CBO9780511618604.

[20] Rezgui A, Cinnella P, Lerat A. Third-order accurate finite volume schemes for Euler computations on curvilinear meshes. Comput Fluids 2005;30(7–8):875–901.

[21] Cinnella P, Congedo P. Aerodynamic performance of transonic Bethe-Zel'dovich-Thompson flows past an airfoil. AIAA J 2005;43(11):2458–61.

[22] Jameson A, Schmidt W, Turkel E. Numerical solution of the Euler equations by finite volume methods using Runge–Kutta time-stepping schemes. AIAA Paper; 1981.

[23] Marin Perez R. Hybrid RANS-LES simulations of turbulent flows in aerodynamics using high-order schemes, Paris, France: Ecole Nationale Supérieure d'Arts et Métiers; 2013. Ph.D. thesis.

[24] Aubard G, Stefanin Volpiani P, Gloerfelt X, Robinet J-C. Comparison of subgrid-scale viscosity models and selective filtering strategy for large-eddy simulations. Flow Turbul Combust. 2013;91(3):497–518.

[25] Gloerfelt X, Cinnella P. Large eddy simulation requirements for the flow over periodic hills. Flow Turbul Combust 2019;103(1):55–91.

[26] Bogey C, Bailly C. A family of low dispersive and low dissipative explicit schemes for flow and noise computations. J Comput Phys 2004;194(1):194–214.

[27] Content C, Outtier P-Y, Cinnella P. Coupled/uncoupled solutions of RANS equations using a Jacobian-free Newton-Krylov method. In: 21st AIAA Computational fluid dynamics conference, AIAA Paper 2013–2423; 2013.

[28] Outtier P, Content C, Cinnella P, Michel B. The high-order dynamic computational laboratory for CFD research and applications. AIAA Paper, 2013–2439; 2013.

[29] Chicheportiche J, Gloerfelt X. Study of interpolation methods for high-accuracy computations on overlapping grids. Comput Fluids 2012;68:112–33.

[30] Kiock R, Lehthaus F, Baines N, Sieverding C. The transonic flow through a plane turbine cascade as measured in four european wind tunnels. J Eng Gas Turb Power 1986;108(2):277–84.

[31] Rubino D, De Palma P, Pascazio G, Napolitano M. Solution of the steady Euler equations using fluctuation splitting schemes on quadrilateral elements. In: Deconinck H, Dick E, editors. Computational fluid dynamics. Springer, Berlin, Heidelberg; 2009. p. 101–6.

[32] Arnone A, Pacciani R. Numerical investigation on wake shedding in a turbine rotor blade. In: Kutler P, Flores J, Chattot J-J, editors. Fifteenth international conference on numerical methods in fluid dynamics. Lecture Notes in Physics, 490. Springer, Berlin, Heidelberg; 1997. p. 358–63.

[33] Grimich K, Michel B, Cinnella P, Lerat A. Finite volume formulation of a third-order residual-based compact scheme for unsteady flow computations. In: Abgrall R, Beaugendre H, Congedo P, Dobrzynski C, Perrier V, Ricchiuto M, editors. High order nonlinear numerical schemes for evolutionary PDEs. Lecture Notes in Computational Science and Engineering, vol. 99. Springer, Cham; 2014. p. 37–58.

[34] Michel B, Cinnella P, Lerat A. Multiblock residual-based compact schemes for the computation of complex turbomachinery flows. Int J Eng SystModell Simul 2011;27(1–2):2–15.

[35] Sieverding H, Richard H, Desse J. Turbine blade trailing edge flow characteristics at high subsonic outlet Mach number. J Turbomach 2003;125(2):298–309.